Support Information

Critical Threshold of 70 mol% CO_2 Concentration for Economically Viable Geological Storage from Direct Air Capture (DAC)

Le Zhang, Yunfeng Liang[*]*, Arata Kioka and Takeshi Tsuji*[*]

Department of Systems Innovation, School of Engineering, The University of Tokyo,
Tokyo 113-8656, Japan

*Corresponding author

E-mail: liang@sys.t.u-tokyo.ac.jp (Y. Liang)

E-mail: tsuji@sys.t.u-tokyo.ac.jp (T. Tsuji)

Method

Temperature and Pressure Range

This work selected 6 well-known CCS projects worldwide. The CarbFix project is a model for CO_2 mineralization research. Reportedly, the injected CO_2 reacts with basalt, achieving permanent disposal within just two years[1,2]. The Cranfield project, located in Mississippi, USA, features high temperature and pressure conditions.[3] Sleipner[4–6] and Decatur[7,8] are among the world's earliest CCS projects, whose designs and processes have served as references for many subsequent projects. Nagaoka is the first Japanese pilot project for CO_2 geological storage[9,10]. The China Offshore project is one of the country's latest CCS initiatives, with significant storage potential[11].

Table S1 Typical CO_2 Storage Site Worldwide

Field Project and Location	Temperature (°C)	Pressure (Bar)
CarbFix, Iceland	20 - 33	~ 60
Cranfield, USA	120	324
Nagaoka, Japan	48	108
Sleipner, Norway	45	100
Decatur IBDP, USA	50	221
China Offshore, China	~90	254

Force Fields

The field force used for CO_2, N_2, and O_2 was from TraPPE-small (Transferable Potential for Phase Equilibria), which is built to calculate small but vital molecules by the University of Minnesota[12,13]. These force fields were used by various studies, showing pretty good agreement in density and vapor-liquid equilibria calculation[14–16]. All Molecules built in TraPPE-small force field have rigid structures (i.e., no bonded potential) and do not otherwise fit into another TraPPE family. Detailed non-bonded parameters and partial charge can be found in Table S2. The Lorentz−Berthelot combination rules were employed to calculate the interactions among molecules. The density calculation uses the isothermal−isobaric (NPT) ensemble to validate the selected force fields for impurities.

Table S2 The Non-bond Parameters for Molecules

Molecules	Atom	$\sigma(nm)$	$\varepsilon(KJ/mol)$	$q(e)$	Critical Temperature(K) TraPPE-model / NIST	Critical Pressure (Bar) TraPPE-model / NIST
CO_2	C	0.2800	0.2244918	0.7000	306.2 / 304.21	77.7 / 73.843
	O	0.3050	0.6568464	-0.3500		
N_2	N	0.3310	0.2993040	-0.4820	126.5 / 126.19	34.6 / 33.98
	MW	0.0000	0.0000000	0.9640		
O_2	O	0.3020	0.4073860	-0.113	153.5 / 154.58	50.63 / 51.1
	MW	0.0000	0.0000000	0.226		

Simulation Details

All Molecule Dynamics (MD) simulations were performed with GROMACS package v2024.4[17]. The particle mesh Ewald (PME) method was applied for both long-range electrostatic and Lennard-Jones interactions with a Fourier spacing of 0.12 nm and a cutoff distance of 1.4 nm[18,19]. The bonds were constrained using a linear constraint solver (LINCS) algorithm with bond constraints added[20]. Additionally, 3-D periodic boundary conditions (PBC) were applied to all simulations. The ratio of N_2 to O_2 in the simulation is kept at 4:1. Each system contains 1,380 molecules. In all simulations, 3-D periodic boundary conditions (PBC) were applied to all simulations. The ratio of N_2 to O_2 in the simulation is kept at 4:1. Each system contains 1,380 molecules. For systems with different CO_2 concentrations, corresponding amounts of CO_2 were replaced with N_2 and O_2 in the same ratio. For example, under the condition of 50 mol%, the system contains 690 CO_2 molecules, 552 N_2 molecules, and 138 O_2 molecules. A total of seven typical cases are considered: 100% (pure CO_2), 95mol%, 90mol%, 80mol%, 70mol%, 60mol%, and 50mol%. A $10 \times 10 \times 10$ nm^3 box was prepared for holding molecules at the beginning stage. The system firstly relaxed through steepest descent algorithm (Energy minimization). After energy minimization, 1-ns NPT simulation with velocity-rescaling thermostat[21] and Berendsen barostat[22] was performed for equilibrium purpose. After that, 5-ns NPT simulation with Nosé-Hoover thermostat and an isotropic Parrinello-Rahman barostat was performed for production[23–25]. Time step was set as 1 fs, so there are 1,000,000 steps for equilibrium and 5,000,000 steps for production runs. Only the last 2 million steps of the final 5 million production simulation steps were used for result analysis, thereby avoiding any early-stage disequilibrium.

Simulation Validation

The density of pure CO_2, N_2, and O_2 are calculated to validate the force field and computational method. Validation cases were conducted at a constant temperature of 325.65 K and varying pressures. The simulation results, presented in Fig. S1, show a strong agreement with NIST WebBook data[26], with an average error of less than 1%. The results confirm the reliability of our simulation methodology and force field for accurate density predictions.

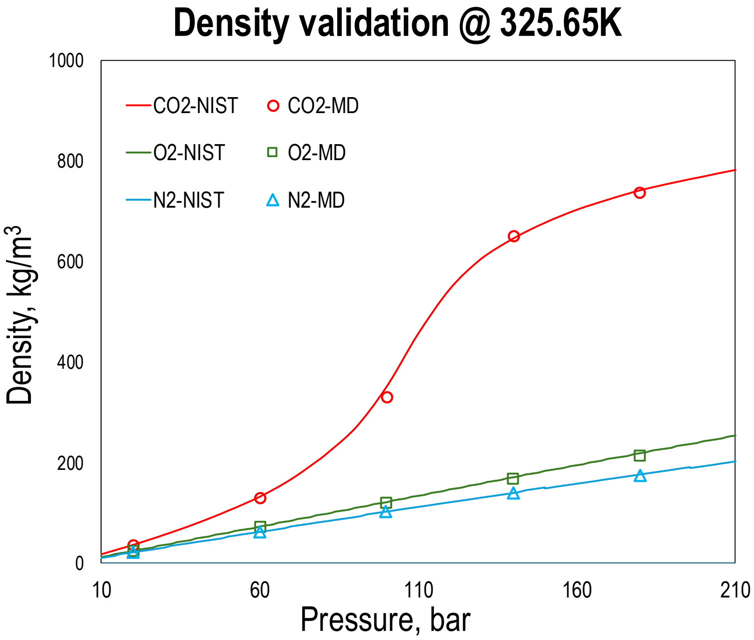

Fig. S1 Density calculation validation results for pure molecules.

Radial Distribution Function (RDF) and Coordination Number Analysis

Besides the Lennard-Jones (LJ) potential and Coulomb potential investigation, we further analyzed the radial distribution functions (RDF) and coordination numbers (CN) for CO_2-CO_2, N_2-N_2, and CO_2-N_2 pairs within the system. Fig. S1 a), d), and g) present the RDF distributions for CO_2-CO_2, N_2-N_2, and CO_2-N_2, respectively. The RDF peak values for different CO_2 concentrations were plotted against temperature, resulting in the curves shown in Fig. S1 b), e), and h). The CN values corresponding to the RDF valley following the first peak were also calculated and are presented in Fig. S1 c), f), and i). The peak data are influenced by concentration, leading to instability. For instance, Fig. S1 e) shows significant fluctuations in the RDF peak of N_2-N_2 under 90% CO_2 conditions, while the CO_2-CO_2 data remain stable. The CN trends displayed in Fig. S1 c), f), and i) reveal that CO_2-CO_2 has a larger slope compared to N_2-N_2 and CO_2-N_2, which show relatively minor changes in slope. A similar trend is observed in the first peak height plots, where the slope changes for N_2-N_2 and CO_2-N_2 are less pronounced. Notably, in the first peak height distribution of CO_2-CO_2, we observed a slope change similar to that in. The difference in values between the right and left sides of the plot is approximately 40.2%, consistent with the previously observed trends in density distribution and LJ potential.

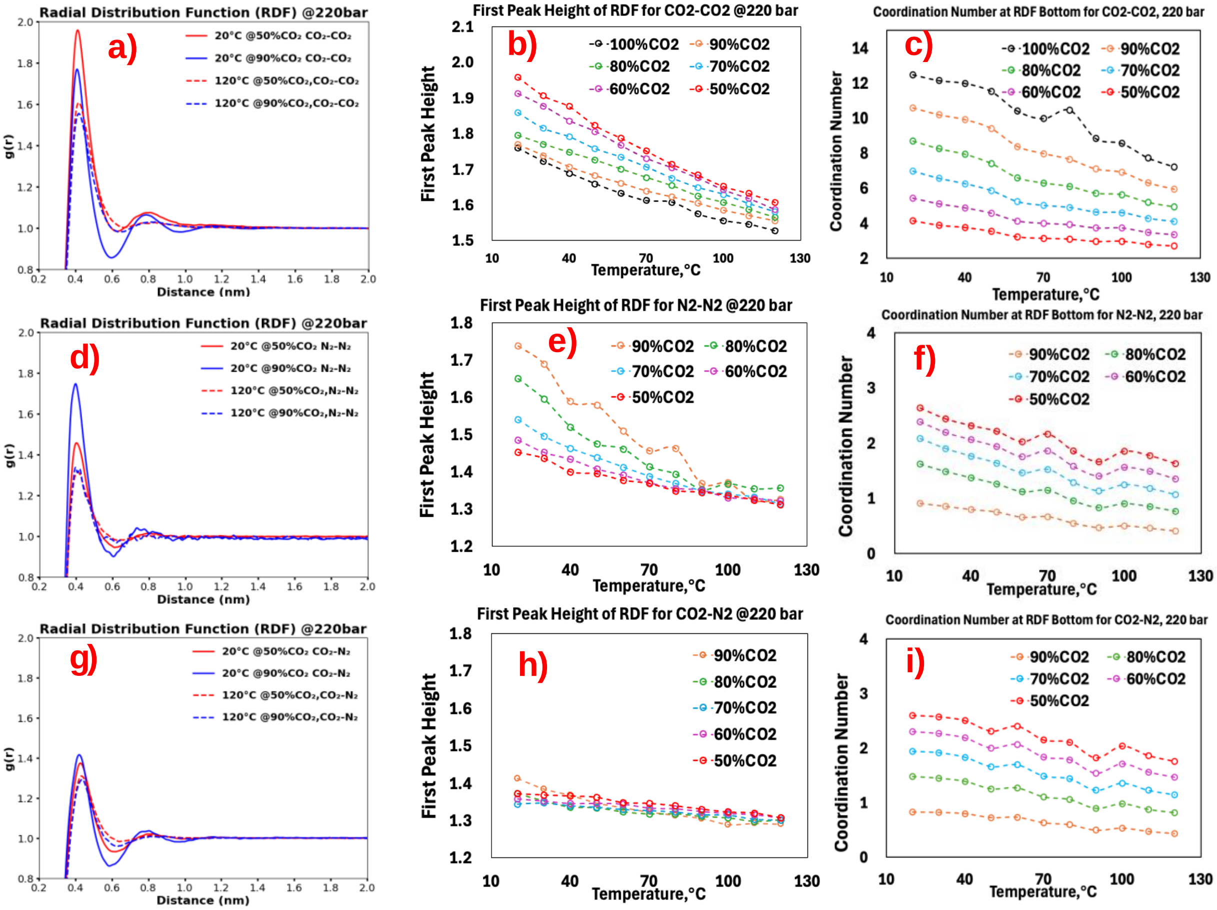

Fig. S1 Radial distribution function (RDF), RDF peak value, and coordination number for CO_2-CO_2, N_2-N_2, and CO_2-N_2.

Temperature and Pressure Gradient Profile

A comprehensive investigation of pressure and temperature was conducted to establish the T-P relation, as shown in Table S3. Saline aquifers, conventional oil and gas reservoirs, shale, and coal beds are considered potential storage formations. In both sandstone and shale reservoirs, the common pressure gradient typically ranges between 90–120 bar/km, However, shale reservoirs in China exhibit higher pressure gradients, likely due to their greater burial depths. The temperature gradient range was not directly derived from the table data; instead, it was determined based on the global temperature distribution of sedimentary basins, making it a more representative selection. The formulas for pressure gradient and temperature gradient are as follows:

$$T - T_0 = K_T \times D \tag{1}$$

$$P = K_P \times D \tag{2}$$

where T_0 is the initial temperature (°C), K_T is the temperature gradient (°C/km), K_P is the pressure gradient (bar/km), and *D* is the depth (km). P-T relation can be obtained by combining these two formulas.

Table S3 Comparison of the Temperature and Pressure Feature for CO_2 Storage Formation

Project and/or Location	Type of Reservoir	Water Depth, m	Temperature gradient, °C/km	Pressure gradient, bar/km	Ref.
Sleipner, Norway	The Utsira, Sandstone	90	33	100~110	4,5
Decatur, USA	Mt. Simon, Sandstone	Onshore	18.2	~103	27,7
Nagaoka, Japan	The Haizume, Sandstone	Onshore	33	98	9,10
Tomakomae, Japan	Volcaniclastic rocks and sand	20~40	~33	92~120	28
In Salah, Algeria	Carboniferous Sandstone	Onshore	~32	~100	29
Louisiana, USA	The Haynesville Shale	Onshore	25~33	103~109	30
South China	The Longmaxi Shale	Onshore	~33	150	31
N/A	A typical sedimentary basin	N/A	30	150	32
Texas, USA	The Barnet Shale	Onshore	~33	~100	33
N/A	A natural Coal Seam	N/A	25	150	34

References

1. Matter, J. M. *et al.* Rapid carbon mineralization for permanent disposal of anthropogenic carbon dioxide emissions. *Science* **352**, 1312–1314 (2016).
2. Zhang, S. & DePaolo, D. J. Rates of CO_2 Mineralization in Geological Carbon Storage. *Acc. Chem. Res.* **50**, 2075–2084 (2017).
3. Lu, J. *et al.* CO_2–rock–brine interactions in Lower Tuscaloosa Formation at Cranfield CO_2 sequestration site, Mississippi, U.S.A. *Chem. Geology* **291**, 269–277 (2012).
4. Arts, R. *et al.* Monitoring of CO_2 injected at Sleipner using time-lapse seismic data. *Energy* **29**, 1383–1392 (2004).
5. Bickle, M., Chadwick, A., Huppert, H. E., Hallworth, M. & Lyle, S. Modelling carbon dioxide accumulation at Sleipner: Implications for underground carbon storage. *Earth Planet. Sci. Lett.* **255**, 164–176 (2007).
6. Zweigel, P., Arts, R., Lothe, A. E. & Lindeberg, E. B. G. Reservoir geology of the Utsira Formation at the first industrial-scale underground CO_2 storage site (Sleipner area, North Sea). *Geological Society, London, Special Publication* **233**, 165–180 (2004).
7. Finley, R. J. An overview of the Illinois Basin – Decatur Project. *Greenh. Gases* **4**, 571–579 (2014).
8. Berger, P. M., Yoksoulian, L., Freiburg, J. T., Butler, S. K. & Roy, W. R. Carbon sequestration at the Illinois Basin-Decatur Project: experimental results and geochemical simulations of storage. *Environ. Earth Sci* **78**, 646 (2019).
9. Sato, K. *et al.* Monitoring and simulation studies for assessing macro- and meso-scale migration of CO_2 sequestered in an onshore aquifer: Experiences from the Nagaoka pilot site, Japan. *Int. J. Greenhouse Gas Control* **5**, 125–137 (2011).

10. Mito, S., Xue, Z. & Ohsumi, T. Case study of geochemical reactions at the Nagaoka CO_2 injection site, Japan. *Int. J. Greenhouse Gas Control* **2**, 309–318 (2008).
11. Li, J. *et al.* Site-Level Carbon Storage Potential Estimation in Offshore China. in *SPE Symposium and Exhibition - Production Enhancement and Cost Optimisation* D021S007R001 (SPE, Kuala Lumpur, Malaysia, 2024). doi:10.2118/220657-MS.
12. Potoff, J. J. & Siepmann, J. I. Vapor–liquid equilibria of mixtures containing alkanes, carbon dioxide, and nitrogen. *AIChE J.* **47**, 1676–1682 (2001).
13. Zhang, L. & Siepmann, J. Ilja. Direct calculation of Henry's law constants from Gibbs ensemble Monte Carlo simulations: nitrogen, oxygen, carbon dioxide and methane in ethanol. *Theor Chem. Acc.* **115**, 391–397 (2006).
14. Aimoli, C. G., Maginn, E. J. & Abreu, C. R. A. Transport properties of carbon dioxide and methane from molecular dynamics simulations. *J. Chem. Phys.* **141**, 134101 (2014).
15. Makimura, D. *et al.* Application of Molecular Simulations to CO_2-Enhanced Oil Recovery: Phase Equilibria and Interfacial Phenomena. *SPE J.* **18**, 319–330 (2013).
16. Yang, X., Feng, Y., Jin, J., Liu, Y. & Cao, B. Molecular dynamics simulation and theoretical study on heat capacities of supercritical H_2O/CO_2 mixtures. *J. Mol. Liquids* **299**, 112133 (2020).
17. Van Der Spoel, D. *et al.* GROMACS: Fast, flexible, and free. *J. Comput. Chem.* **26**, 1701–1718 (2005).
18. Petersen, H. G. Accuracy and efficiency of the particle mesh Ewald method. *J. Chem. Phys.* **103**, 3668–3679 (1995).

19. Wennberg, C. L., Murtola, T., Hess, B. & Lindahl, E. Lennard-Jones Lattice Summation in Bilayer Simulations Has Critical Effects on Surface Tension and Lipid Properties. *J. Chem. Theory Comput.* **9**, 3527–3537 (2013).

20. Hess, B., Bekker, H., Berendsen, H. J. C. & Fraaije, J. G. E. M. LINCS: A linear constraint solver for molecular simulations. *J. Comput. Chem.* **18**, 1463–1472 (1997).

21. Berendsen, H. J. C., Postma, J. P. M., Van Gunsteren, W. F., DiNola, A. & Haak, J. R. Molecular dynamics with coupling to an external bath. *J. Chem. Phys.* **81**, 3684–3690 (1984).

22. Bussi, G., Donadio, D. & Parrinello, M. Canonical sampling through velocity rescaling. *J. Chem. Phys.* **126**, 014101 (2007).

23. Hoover, W. G. Canonical dynamics: Equilibrium phase-space distributions. *Phys. Rev. A* **31**, 1695–1697 (1985).

24. Parrinello, M. & Rahman, A. Strain fluctuations and elastic constants. *J. Chem. Phys.* **76**, 2662–2666 (1982).

25. Nosé, S. A molecular dynamics method for simulations in the canonical ensemble. *Mol. Phys.* **100**, 191–198 (2002).

26. Lemmon, E. W. Thermophysical Properties of Fluids. *NIST* (2009).

27. Senel, O., Will, R. & Butsch, R. J. Integrated reservoir modeling at the Illinois Basin – Decatur Project. *Greenh. Gases* **4**, 662–684 (2014).

28. Tanaka, Y. *et al.* Tomakomai CCS Demonstration Project of Japan, CO_2 Injection in Process. *Energy Procedia* **114**, 5836–5846 (2017).

29. Rutqvist, J., Vasco, D. W. & Myer, L. Coupled reservoir-geomechanical analysis of CO_2 injection and ground deformations at In Salah, Algeria. *Int. J. Greenhouse Gas Control* **4**, 225–230 (2010).

30. Nunn, J. A. Burial and Thermal History of The Haynesville Shale: Implication For Overpressure, Gas Generation, and Natural Hydrofracture. *Geol. Soc. (GCAGS) J.* v.1, 2012.
31. Pan, L., Xiao, X., Tian, H., Zhou, Q. & Cheng, P. Geological models of gas in place of the Longmaxi shale in Southeast Chongqing, South China. Mar. Petrol. Geology 73, 433–444 (2016).
32. Zhang, H. & Cao, D. Molecular simulation of displacement of shale gas by carbon dioxide at different geological depths. *Chem. Eng. Sci.* **156**, 121–127 (2016).
33. Tang, X., Ripepi, N., Stadie, N. P., Yu, L. & Hall, M. R. A dual-site Langmuir equation for accurate estimation of high pressure deep shale gas resources. *Fuel* **185**, 10–17 (2016).
34. Li, X., Sun, X., Walters, C. C. & Zhang, T. H_2, CH_4 and CO_2 adsorption on Cameo coal: Insights into the role of cushion gas in hydrogen geological storage. *Int. J. Hydro. Energy* **50**, 879–892 (2024).